

# Bunch Compressor Design for the APS Linac

M. Borland  
AOD/OAG

## *Abstract*

A bunch compressor is required for the APS linac in order to produce higher peak currents for the LEUTL FEL. Peak currents of 300 to 600A are desirable with normalized emittances of about 5 mm-mrad. In addition, compression to higher peak currents is interesting in order to explore the physics of coherent synchrotron radiation (CSR) in the compressor itself, a topic of great interest to designers of the LCLS. This note discusses the physics design of a compressor that satisfies these requirements. Simulations use the program **elegant** and include CSR effects in the chicane dipoles and drifts, as well as longitudinal and transverse wakefields.

## 1.0 Overview

The APS bunch compressor design is an outgrowth of design studies[1] by P. Emma and V. Bharadwaj of SLAC. They proposed a number of possible chicane designs, including symmetric and asymmetric four-dipole chicanes. Based on this work, I undertook more detailed simulations using **elegant** which indicated a considerable advantage in the asymmetric design, specifically one in which the two downstream dipoles of the chicane are about half the strength of the two upstream dipoles.

The work of Emma and Bharadwaj assumed compression to 600A of a 1nC photoinjector beam using a chicane with  $R_{56} = 38mm$ . Because the CSR-induced emittance growth depends on the strength of the dipoles, I explored the effect of using different values of  $R_{56}$ . Configurations were obtained for a range of  $R_{56}$  and varying degrees of asymmetry, under the assumption that the chicane would be constructed with moving magnets and flexible vacuum chambers. For many of these configurations, detailed longitudinal and transverse optimizations were carried out to allow evaluation of emittance growth and error sensitivities. One result of these studies is that sensitivities vary considerably between configurations, depending on the beam performance required. This provides another motivation for a system with variable  $R_{56}$ .

For purposes of this note, the APS linac is considered to consist of 5 parts:

1. The photoinjector, which delivers a beam of 0.5-1nC at about 43MeV. The photoinjector extends from the photocathode gun to the end of linac section 1. Simulations of the photoinjector are performed by J. Lewellen (ASD/PHY) using PARMELA.
2. The precompressor linac, which consists of four SLAC-type accelerating waveguides driven by a single SLEDed klystron. The phase and voltage of this section, called L2, are adjusted to achieve the desired energy in the compressor and the desired bunch length after the compressor. The waveguides have large-bore quadrupoles around them which provide focusing of the beam. Energies of up to 210 MeV are possible at this point, but I have limited myself to 185 MeV to be conservative.
3. The bunch compressor, which consists of a four-magnet chicane, quadrupoles, and diagnostics for emittance measurement and characterization of CSR.
4. The post-compressor linac, which consists of eight SLAC-type accelerating waveguides in two groups (called L4 and L5) of four. Each group of four waveguides is driven by a single SLEDed klystron. The phase and voltage of these waveguides are adjusted to obtain the desired final energy and minimize the final energy spread. Again, the waveguides have large-bore quadrupoles around them to provide beam focusing. Energies of up to 700 MeV are possible at this point, but the highest energy of interest for these studies is about 460 MeV.
5. The post-linac transport line to the PAR-bypass emittance measurement section. This consists of seven quadrupoles that are part of the LTP and PAR-bypass lines, ending at the first screen (called PB:FL:C1) of a three-screen emittance measurement section. This screen is the endpoint of the simulations, where I evaluate beam properties and stability.

## 2.0 Modeling of Wakefields

Longitudinal and transverse wakefields can have a major impact on beam parameters and beam quality in linacs with high peak currents. Longitudinal wakefields are partially correctable via proper phasing of the linac, at some cost in total acceleration. Transverse wakefields can be controlled by keeping the beam centered in the accelerating sections.

A similar technique is used to model both types of wakes. Consider first a single exciting particle trailed by a single probe particle. For longitudinal wakes, the effect on the probe particle trailing the exciting particle with charge  $q$  at a distance  $z$  is

$$\Delta\gamma = \frac{qW(z)}{0.511 \cdot 10^6}$$

In the simulation, the wake  $W(z)$  is supplied as a table of numbers (see below). The bunch longitudinal profile is binned to make a histogram  $H(z)$ , with a bin size equal to the point spacing of the wake function table. This histogram is convolved with the wake function and multiplied by  $q/(0.511 \cdot 10^6)$  to obtain  $\Delta\gamma(z)$ . The convolution is performed explicitly, rather than using FFTs, since the wake function is not periodic. This gives

$\Delta\gamma(z)$  at discrete  $z$  values, with the same spacing as the table of wake function values. **elegant** interpolates this table to obtain the  $\Delta\gamma$  for each particle. In changing the energy of the particle, the slopes of the trajectories must be changed to keep the transverse momenta constant.

For the transverse wake, the procedure is similar. for simplicity, consider the  $x$  plane only. (The  $y$  plane is independent and is handled in the same fashion.) In this case, the transverse kick delivered to the trailing particle is

$$\Delta x' = \frac{qxW_x(z)}{p_z 0.511 \cdot 10^6}$$

where  $x$  is the transverse position of the drive particle and  $p_z$  is the longitudinal momentum of the probe particle.

In the simulation, an  $x$ -weighted histogram of longitudinal density is made. This histogram is then convolved with the transverse wake function to give  $p_z \Delta x'(z)$ . For each simulation particle **elegant** interpolates this function at the appropriate  $z$  and divides by the particle's longitudinal momentum to obtain the transverse kick.

The wake functions are supplied by P. Emma[3] as tables of numbers vs distance behind the exciting charge. The longitudinal wake function gives V/C/cell as a function of distance behind the exciting particle, while the transverse wake function gives V/C/m/cell as a function of distance behind the exciting particle.

In the simulation runs, I employed one longitudinal wake element per 3m accelerating section, in order to economize computer time. This is a good approximation for relativistic particles. For the transverse wake, I used an average of 18 transverse wake kicks per 3m section. This was determined primarily by the way I split the accelerating sections into RFCA elements, as I placed one transverse wake element after each RFCA element.

## 3.0 Modeling of CSR

### 3.1 CSR in Dipoles

The CSR model used by **elegant** is based on the theoretical work on Saldin, et. al. [4], where an equation is given for the energy change of a line charge distribution as a function of the position in the bunch and in a bending magnet:

$$\frac{dE}{d(ct)} = \frac{-2e^2}{(3R^2)^{1/3}} \left\{ \frac{1}{s_l^{1/3}} [\lambda(s-s_l) - \lambda(s-3s_l)] + \int_{(s-s_l)}^s \frac{1}{(s-s')^{1/3}} \frac{d\lambda(s')}{ds'} ds' \right\}$$

where  $s_l = \frac{R\phi^3}{24}$  is the “slippage length”,  $\phi$  is the angle position in the dipole, R is the bending radius, s is the position of a particle in the bunch, and ct is the position of the center of the bunch.  $\lambda(s)$  is the linear density distribution of the bunch, such that

$$\int_{-\infty}^{\infty} \lambda(s) ds = 1 .$$

This function giving the energy change along the bunch is referred to as

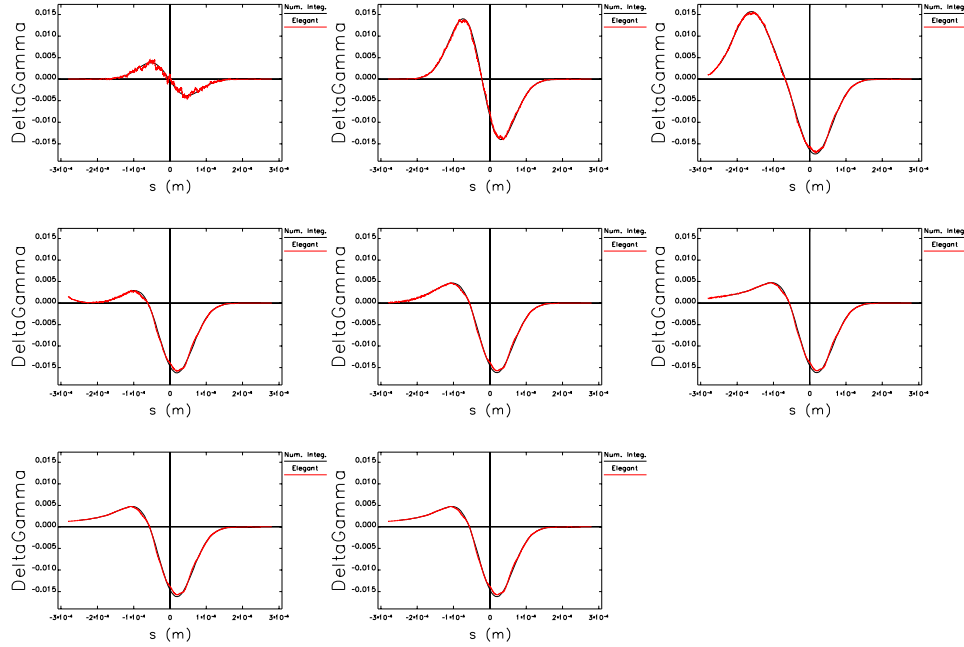
the “CSR wake,” although, unlike true wakefields, with CSR a particle can be affected by particles behind it.

I modified **elegant** to incorporate this equation into a version of the existing CSBEND (Canonical Sector BEND) element. This element uses a second- or fourth-order canonical integrator[5] to model a dipole. The modified element (CSRCSBEND) includes CSR energy kicks along with the dipole field kicks in the integration. Typically, the dipole is integrated using 100 steps. For each step, the CSR effects are computed as follows:

1. Particle arrival times at the end of the dipole piece are binned. About 3000-4000 bins are recommended for 10000 particles in a gaussian distribution. The bin size is automatically adjusted to encompass the entire beam plus 10% empty buffer space at the ends.
2. The density histogram is smoothed using FFT convolution with a Savitzky-Golay filter[6]. The parameters of the smoothing are user controlled, but I typically smooth over +/- 50 bins using a linear fit order.
3. The same filter is used to take the derivative of the smoothed density.
4. The function  $\frac{dE}{d(ct)}$  is computed for each bin using simple sums for the integration.
5. Each particle’s energy is changed according the value of  $\frac{dE}{d(ct)}$  for the bin it occupies.

**elegant** optionally provides the user with the linear density, its derivative, and the CSR wake at points along the dipole. This output was used to check the implementation. In particular, I compared tracking results for a model gaussian beam to those in Saldin, et. al., and to my own numerical computation for a gaussian. The agreement was very good, as shown in Figure 1. The parameters were 1nC, 50um bunch length, and 1.5m bending radius.

**FIGURE 1. Comparison of numerical integration of CSR wake for a gaussian bunch with elegant's computation.**



### 3.2 CSR in Drifts

To model CSR in drifts, I make the following plausible assumptions:

1. The CSR created at the end of the dipole travels at the speed of light on the beam path through the following drift space.
2. The CSR wakefield does not change shape (i.e.,  $z$  dependence) as it travels.
3. The CSR wakefield spreads transversely as it travels, just as any synchrotron radiation does, according to the formula[7]

$$\sigma_{x, rad}(z) = \sqrt{\Sigma_{11} + 2\Sigma_{12}z + (\Sigma_{22} + \sigma_{rad}^2)z^2}$$

where  $z$  is the distance from the end of the dipole,  $\sigma_{x, rad}$  is the radiation beamsize,  $\Sigma$  is the electron beam matrix at  $z = 0$ .  $\sigma_{rad}$  is the gaussian opening angle of the radiation, given by[8]

$$\sigma_{rad} = \frac{0.00055}{\left(\frac{\lambda_c}{\lambda}\right)^{1/3}} E$$

where  $\lambda_c$  is the critical wavelength,  $E$  is the energy in MeV, and  $\lambda$  is the radiation wavelength.

4. The radiation wavelength,  $\lambda$  is equal to the RMS bunch length,  $\sigma_z$ , for a gaussian beam, and equal to half the 68% beam length for a nongaussian beam.
5. The intensity of the wake varies due to spreading by the ratio of the initial radiation beamsize to the radiation beamsize at  $z$

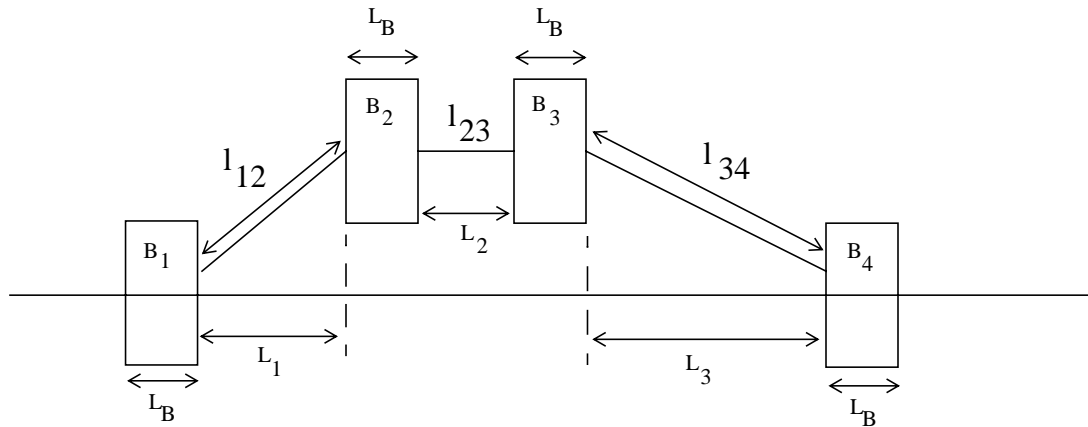
$$\frac{\sigma_{x, rad}(0)}{\sigma_{x, rad}(z)}$$

Based on these assumptions, **elegat** saves the CSR wake at the end of each CSRCS-BEND element, and uses it in any CSRDRIFT elements that follow. It then uses that CSR wake just as it does for a dipole, to modify the energy of each particle in the beam.

While this method is clearly not rigorous, it gives results in reasonable agreement with those of rigorous codes, based on results from such codes reported by P. Emma[3]. Without some way to model CSR in drifts, **elegat** clearly underestimates the effect of CSR.

## 4.0 Chicane Configurations

FIGURE 2. Chicane Nomenclature



The four-magnet chicane has two adjustable parameters: the value of  $R_{56}$  and the “asymmetry,” which is the ratio of the distance between the third and fourth dipoles (B3 and B4) to the distance between the first and second dipoles (B1 and B2). This ratio varies from 1 (symmetric) to about 2. Figure 1 illustrates the quantities involved in setting up chicane

configurations. The asymmetry is  $\frac{L_3}{L_1}$ . There is no particular meaning to this quantity;

in retrospect  $\frac{\theta_1}{\theta_4}$  would have been a better choice, where  $\theta_1 = -\theta_2$  is the bend angle of the first dipole and  $\theta_4 = -\theta_3$  is the bend angle of the last dipole.

Setting up a configuration consists of choosing the desired  $R_{56}$  and asymmetry. Based on this, an initial value of  $L_3$  is computed ( $L_1$  being fixed). This is used to compute  $\theta_1$  using

$$\theta_1 \cong \sqrt{\frac{-R_{56}}{L_1 + \frac{2}{3}L_B + \left(\frac{L_1}{L_3}\right)^2 \left(L_3 + \frac{2}{3}L_B\right)}}$$

(Note that  $R_{56}$  is negative for a compressor.) A starting value of  $\theta_4$  is computed using

$$\theta_4 = \text{asin}\left(\frac{L_1 + L_B}{L_3 + L_B} \cdot \sin\theta_1\right)$$

Finally, a consistent value of  $L_3$  is computed using

$$L_3 = \frac{L_1 \tan\theta_1 + 2\rho_1(1 - \cos\theta_1) - 2\rho_3(1 - \cos\theta_3)}{\tan\theta_3}$$

Given these values as a starting point, I use elegant to match the chicane in three steps

1. Match for the desired  $R_{56}$  while keeping at zero  $R_{16}$  and the offset of the output trajectory from the initial trajectory. This is done by varying  $l_{34}$ ,  $\theta_1$ , and  $K_1$  for the first “tweaker” quad (between B1 and B2), while keeping a fixed ratio between  $\theta_1$  and  $\theta_4$  (to maintain the desired asymmetry). The edge angles are also varied to retain rectangular-magnet conditions, and the arc length of the dipoles are varied to retain the

fixed value of  $L_B$ . In addition, the arc distance between the end of B1 and the upstream tweaker quad (Q1) is varied to keep the center of the magnet a constant distance from the center of B1. This is accomplished by changing the drift distance between B1 and Q1 according to

$$l_{1Q} = \sqrt{(L_{CQ} \cdot \sin\theta_1 - \rho_1 \cdot (1 - \cos\theta_1))^2 + \left(\frac{L_B}{2} + L_{CQ} \cdot \cos\theta_1 - \rho_1 \sin\theta_1\right)^2} - \frac{l_Q}{2}$$

where  $L_{CQ} = 0.258m$  is the distance from the dipole center to the quad center and  $l_Q = 0.076m$  is the length of the quad. The same is done for the downstream tweaker quad (Q2) between B3 and B4. The drift spaces from Q1 (Q2) to B2 (B4) are adjusted to maintain the correct total distance from B1 to B2 (B3 to B4).

2. The optimization is repeated, but with  $K_1$  for Q2 added to the variables and  $R_{26}=0$  added to the constraints. This two-step approach was found to provide slightly better results than having Q2 and  $R_{26}$  in the optimization from the start.
3. The drift space following B4 is adjusted to fit within a defined total length.

As a check of the configurations, each configuration is reloaded into **elegant** to compute the matrix and the survey coordinates. This procedure demonstrates that the matching conditions were very well satisfied. For example, the residual values of  $R_{16}$ ,  $R_{26}$ , and the trajectory offset and angle were  $2 \cdot 10^{-9}$  or less (in meters or dimensionless, as appropriate).

## 5.0 Longitudinal Matching

For a given desired peak current, a wide range of  $R_{56}$  values may be used. Smaller  $|R_{56}|$  requires larger energy spread, which in general one would consider undesirable. However, smaller  $R_{56}$  also implies smaller bending angles and hence weaker CSR-induced emittance growth, which is desirable. In addition, jitter studies show that factors of 2 or 3 in phase and voltage jitter tolerances may be gained by suitable choice of  $R_{56}$ . Hence, there are many reasons to try different values of  $R_{56}$ .

**TABLE 1. Desired Beam Parameters for Linac with Bunch Compressor**

Energy (MeV)	Peak Current (A)	Energy Spread (%)	Normalized Emittance (mm-mrad)	Charge (nC)
217	300	<0.1%	5	0.5
457	600	<0.15%	5	0.5

Steve Milton[2] has specified the desired performance characteristics for LEUTL operation. These are listed in Table 1. I'll refer to these two sets of properties as the 300A and 600A cases. To define the peak current, I make use of the "80% bunch length",  $\Delta t_{80}$ , which is simply the difference between the 90th percentile time-of-flight and the 10th percentile time-of-flight. The peak current is defined as  $\frac{0.8Q}{\Delta t_{80}}$ , where Q is the total charge in

the bunch. This figure provides a more realistic computation of current than using an RMS quantity, which can be corrupted by tails or spikes in the distribution.

In addition to  $R_{56}$ , there are two other variables that one may choose in achieving these goals: the first being the asymmetry of the chicane and the second the energy at the bunch compressor. Having chosen these, the optimization proceeds in several stages in an automated fashion.

1. Prepare the PARMELA output beam for use with **elegant**. This is done once for all the simulations. The PARMELA beam is drifted backwards 1.2m to the exit flange of L1. It is also filtered to remove particles with large radii; the criterion used was to remove the upper 7% of the radius distribution. This leaves about 47K particles for tracking. The particles are each assigned a charge of 0.5nC/50000. The particles used were actually generated by a PARMELA simulation for 1nC. However, I chose to use these particles for 0.5nC because it will slightly overestimate the emittance and is hence conservative.
2. Optimize the phase and voltage of the precompressor linac to obtain the desired peak current and intermediate energy. This involves repeated tracking of the prepared photoinjector bunch through the precompressor linac and the chicane. Longitudinal wakefields are included in the linac but CSR is not included in the compressor. I found in the course of the simulations that the bunch will decompress in the postcompressor linac due to velocity spread brought about by the significant energy spread, resulting in lower peak current at the end of the linac. Hence, for the 300A (600A) case, I optimize to 310A (626A) at this stage. This results in close to the desired final peak current, and consistent values of peak current in the bunch compressor. It is assumed in this step that the two parts of the postcompressor linac (L4 and L5) are run at the same voltage and phase.
3. Optimize the phase and voltage of the postcompressor linac to obtain the minimum energy spread and the desired final energy. In this case, tracking starts from the opti-

mized result of step 1, so that only the postcompressor linac is simulated. Again, longitudinal wakefields are included.

4. Combine the optimized parameters from steps 1 and 2, then track through the entire linac and bunch compressor with wakefields. Again, CSR is not included (since for one thing the transverse matching hasn't been done and it will impact CSR). This step serves to check the results prior to use in other stages. Typically, the difference in the 80% bunch length between the end of step 2 and this step is about 0.1fs. (The agreement is imperfect because **elegant** keeps the full time-of-flight of all particles, so that bunch length is computed from the differences between relatively large quantities. The exact value of the 80% time length is sensitive to small errors. In contrast, the RMS time length is the same in the two cases to within  $10^{-20}$  s.)

Steps 2 through 4 are executed by a single run of **elegant**, so that no human interaction is required other than reviewing the results. A typical run takes several hours to complete, since each evaluation of the optimization function requires tracking about 50k particles with rf and wakefields. Results of the runs will be summarized in the next section.

## 6.0 Transverse Matching

Once the longitudinal matching is completed, transverse matching can take place. This is done for each longitudinal configuration separately. The transverse matching runs start by loading the final longitudinal matching results from the appropriate parameter save file produced by **elegant**. A setup script is used to create a file with only the desired parameters.

For all longitudinal configurations, I started with the same set of quadrupole strengths (K1). These were derived from earlier runs and hence served as a good starting point. The origin of the lattice design was iterative manual adjustment of the quadrupoles using a script that ran **elegant** and displayed the Twiss parameters. Having done this once, I found that a staged matching approach allowed matching a new configuration with no human involvement. Because I started close to a good solution, I was able to include more variables in each stage than would normally be sensible.

The initial beta functions were obtained using the **tellipse** program to analyze the filtered PARMELA data. It simply computes the sigma matrix and then the beta functions. The values are  $\beta_x = 4.03m$ ,  $\alpha_x = -1.61$ ,  $\beta_y = 4.20m$ , and  $\alpha_y = -1.65$ . The steps in the matching are summarized here:

1. Simulate from the end of L1 to the beginning of L4. Vary L1:QM1 through L1:QM5 and L2:QM1 through L2:QM8. Constrain maximum beta functions to 20m. Require alternating  $\beta_x > \beta_y$  and  $\beta_y > \beta_x$  conditions at L2 QMs, vertical beta waist at L3:PM2 (between B2 and B3) with  $\beta_y < 5m$ , and horizontal beta waist at the entrance of L3:BM4 with  $\beta_x < 5m$ .

2. Simulate from the end of L1 to the beginning of L4. Vary L2:QM5 through L2:QM8 and L3:QM3 through L3:QM6. Relax waist constraints of previous step to simply require horizontal (vertical) beta of less than 5m (10m) at L3:BM4 (L3:PM2) entrance. Add constraint in emittance measurement section to obtain 60 degrees betatron phase advance in both planes between successive screens. This tuning was suggested by P. Emma[3] and found to provide better performance in the presence of measurement error. For three screens spaced by 1m, the matching condition at the first screen is

$$\beta = \sqrt{3} + \frac{1}{\sqrt{3}} \text{ and } \alpha = \sqrt{3}.$$

3. Simulate from the start of L4 to PB:FL:C1. Vary PL:QMs 2, 3, 4, 5, 8, 11, 14, 17, 20, 22, and 24. Constrain maximum beta functions to 30m. Require alternating high/low  $\beta_x$  and  $\beta_y$  at the PL:QM with values of 11m and 15m. Require approximate beta and alpha values at the end of L5 to get decent matching through the LTP to PB:FL:C1.
4. Simulate from the start of L4 to PB:FL:C1. Vary LTP:Q10 through LTP:Q6, plus PB:Q1 and PB:Q2. Constrain maximum beta function to 35m. Match to  $\beta = 9.6m$  and  $\alpha = 1$  at PB:FL:C1 for both planes. Because they are very weak, LTP:Q6 and LTP:Q7 are constrained to have strengths at least equivalent to the measured residual gradient after standardization.
5. Track from the end of L1 to PB:FL:C1, including CSR and longitudinal wakefields.

This procedure is accomplished using five runs of **elegant** for each longitudinal configuration. Each run automatically loads the required values from the previous run and the longitudinal matching run. Figure 1 shows a typical set of beta functions.

FIGURE 3. Beta functions for the 300A case with  $R_{56} = 65\text{mm}$  and asymmetry of 1.

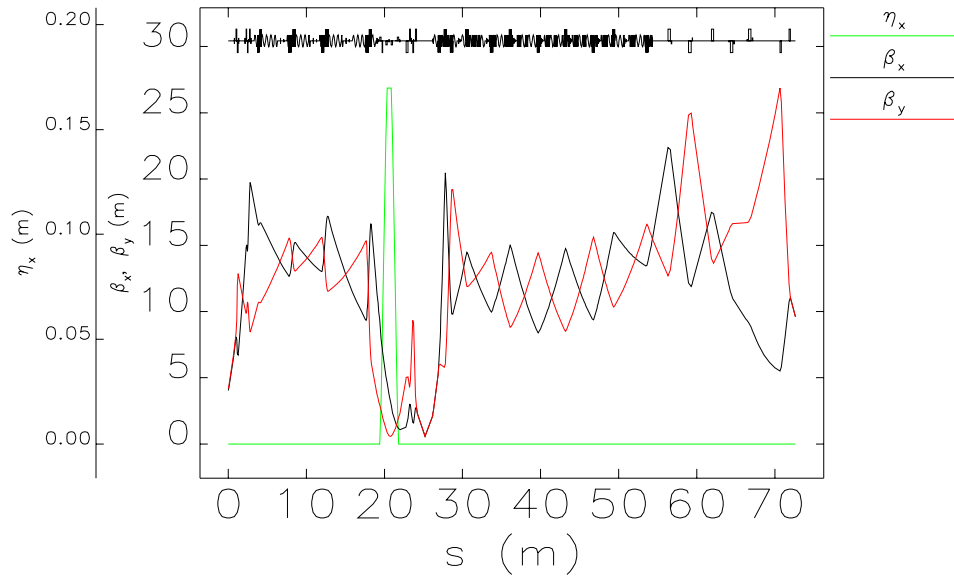
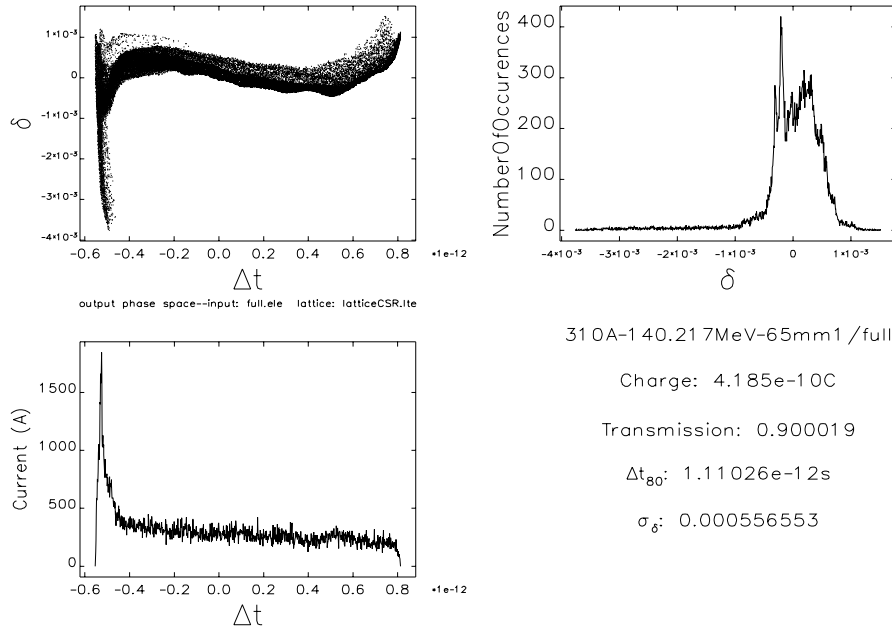


FIGURE 4. Longitudinal phase space for 300A case with  $R_{56} = 65\text{mm}$  and asymmetry of 1.



I wrote several scripts to postprocess the results of these runs. One of these summarizes the beam parameters, as listed in Table 2. The “Run ID” is composed of the target current

(at the end of the bunch compressor), the intermediate energy (140 or 185 MeV), the final energy (217 or 457 MeV),  $R_{56}$ , and the asymmetry (1 or 2).

Figures 5 and 6 show the final horizontal emittance as a function of  $R_{56}$  for the symmetric and asymmetric cases. The different trends for the 600A case are interesting and counterintuitive. One hypothesis is that the symmetric cases suffer from greater emittance growth due to chromatic aberrations, which is expected to worsen at lower  $R_{56}$ . However, simulations without CSR show that this emittance growth, while present, is too small to account for the observed trend. Another hypothesis is that variations in the matching result in differences in the CSR-induced growth between bends; this hypothesis is plausible because we know that the CSR-induced emittance growth in the bends must be lower for lower  $R_{56}$ . However, this hypothesis has not been tested.

**FIGURE 5. Horizontal emittance vs  $R_{56}$  for asymmetry 1 configurations. Each point is labeled with the peak current in amps.**

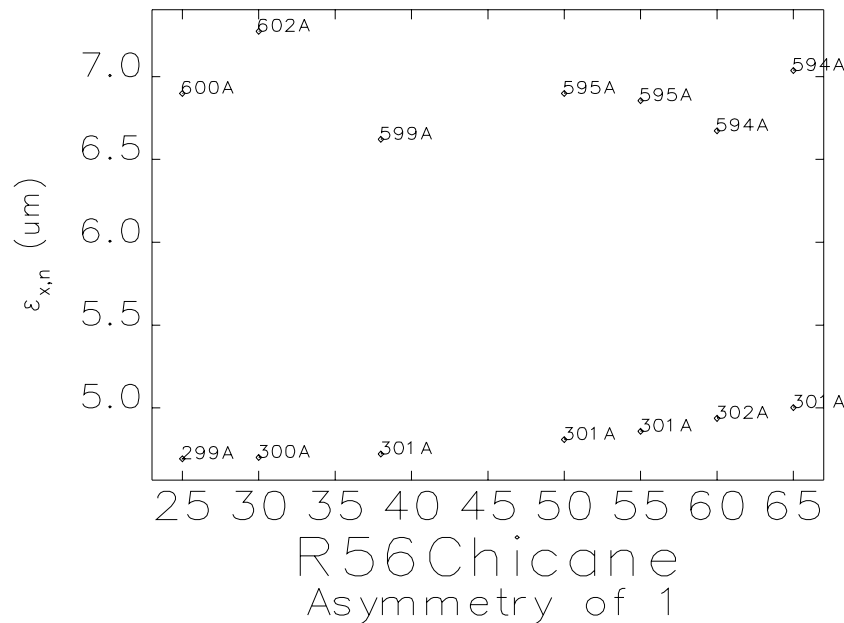
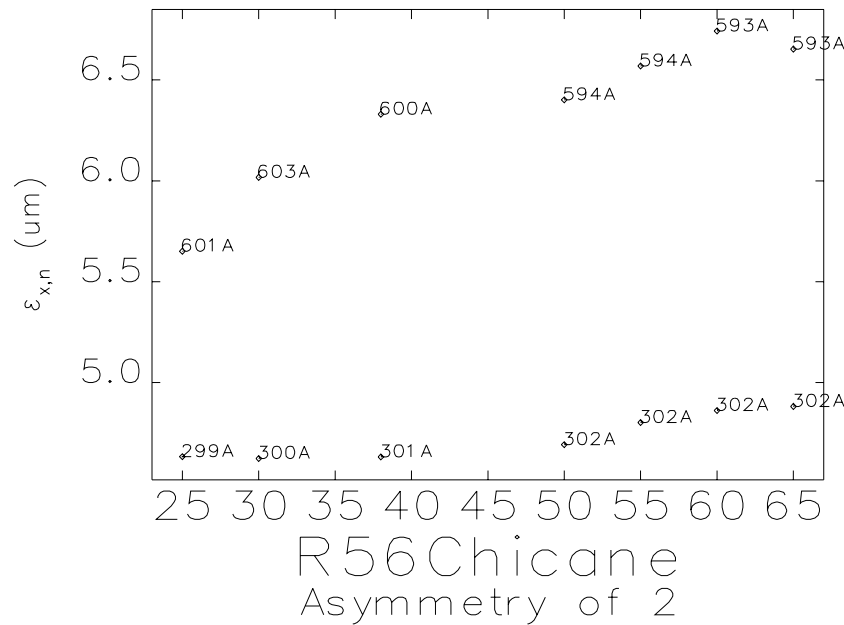


**FIGURE 6. Horizontal emittance vs  $R_{56}$  for asymmetry 2 configurations. Each point is labeled with the peak current in amps.**



The trends in the final current are interesting (see Figures 7 and 8): for the 300A cases, the current increases slightly with  $R_{56}$ , while for the 600A cases, it decreases slightly. This results from a combination of CSR effects and the increase in energy spread required when the  $R_{56}$  is reduced. The results without CSR show the same trend for both 300A and 600A cases, namely, that there is less decompression (from 310A or 626A) with higher  $R_{56}$ . CSR adds more energy spread for the higher  $R_{56}$  values (stronger bends), hence enhancing the decompression.

**FIGURE 7. Current vs  $R_{56}$  for 300A cases.**

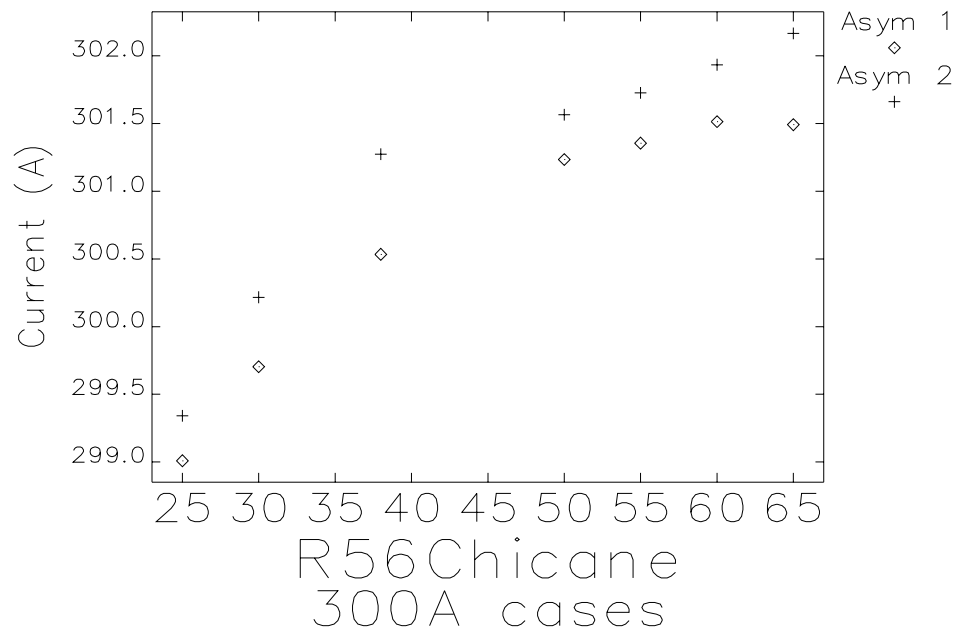


**FIGURE 8. Current vs  $R_{56}$  for 600A cases.**

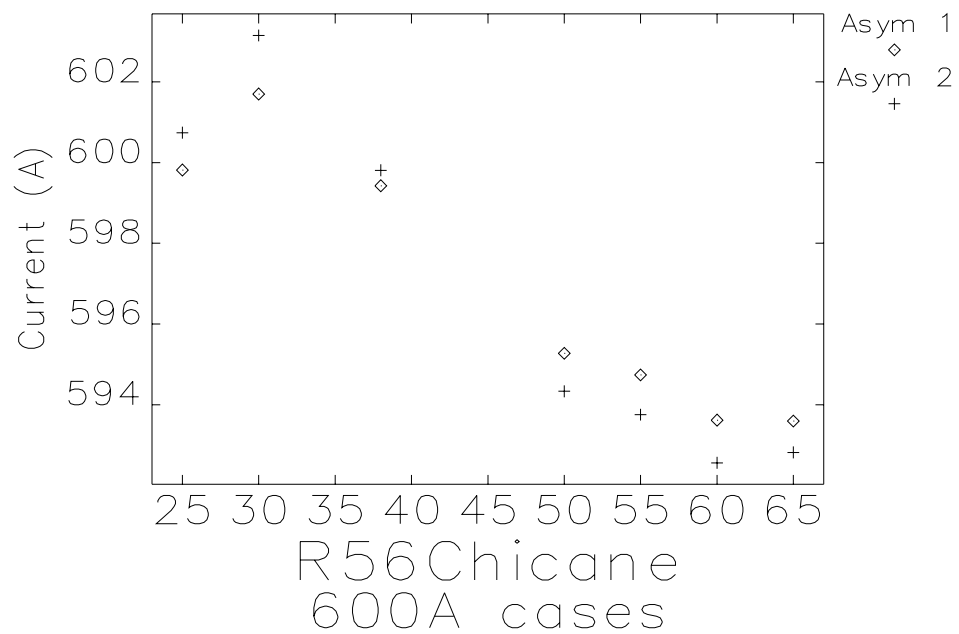


**TABLE 2. Results of tracking through the matched configurations for different values of  $R_{56}$  and asymmetry.**

<b>Current (A)</b>	$\Delta t_{80}$ (ps)	$\sigma_{\delta}$ (%)	<b>Q (nC)</b>	$\epsilon_{nx}$ ( $\mu m$ )	$\epsilon_{ny}$ ( $\mu m$ )	<b>Run ID (see text)</b>
299.01	1.120	0.076	0.418	4.694	4.658	310A-140.217MeV-25mm1
299.34	1.118	0.077	0.418	4.633	4.668	310A-140.217MeV-25mm2
299.70	1.117	0.065	0.418	4.702	4.600	310A-140.217MeV-30mm1
300.22	1.115	0.066	0.418	4.625	4.588	310A-140.217MeV-30mm2
300.53	1.114	0.056	0.418	4.723	4.533	310A-140.217MeV-38mm1
301.27	1.111	0.056	0.418	4.632	4.525	310A-140.217MeV-38mm2
301.24	1.111	0.052	0.418	4.809	4.482	310A-140.217MeV-50mm1
301.57	1.110	0.054	0.418	4.693	4.478	310A-140.217MeV-50mm2
301.36	1.111	0.052	0.418	4.860	4.469	310A-140.217MeV-55mm1
301.73	1.110	0.054	0.418	4.802	4.474	310A-140.217MeV-55mm2
301.51	1.110	0.053	0.418	4.937	4.462	310A-140.217MeV-60mm1
301.93	1.109	0.056	0.418	4.862	4.468	310A-140.217MeV-60mm2
301.49	1.110	0.055	0.418	5.003	4.451	310A-140.217MeV-65mm1
302.17	1.108	0.060	0.418	4.883	4.451	310A-140.217MeV-65mm2
599.82	0.558	0.174	0.418	6.897	4.745	626A-185.457MeV-25mm1
600.74	0.557	0.176	0.418	5.652	4.701	626A-185.457MeV-25mm2
601.70	0.556	0.146	0.418	7.273	4.639	626A-185.457MeV-30mm1
603.16	0.555	0.150	0.418	6.017	4.635	626A-185.457MeV-30mm2
599.43	0.559	0.119	0.418	6.621	4.555	626A-185.457MeV-38mm1
599.81	0.558	0.127	0.418	6.330	4.551	626A-185.457MeV-38mm2
595.27	0.562	0.106	0.418	6.897	4.499	626A-185.457MeV-50mm1
594.33	0.563	0.113	0.418	6.401	4.494	626A-185.457MeV-50mm2
594.74	0.563	0.104	0.418	6.854	4.486	626A-185.457MeV-55mm1
593.75	0.564	0.110	0.418	6.569	4.478	626A-185.457MeV-55mm2
593.62	0.564	0.102	0.418	6.672	4.475	626A-185.457MeV-60mm1
592.56	0.565	0.109	0.418	6.742	4.464	626A-185.457MeV-60mm2
593.59	0.564	0.103	0.418	7.035	4.461	626A-185.457MeV-65mm1
592.82	0.565	0.108	0.418	6.653	4.455	626A-185.457MeV-65mm2
1107.59	0.605	0.106	0.837	11.416	4.457	1200A-185.457MeV-65mm1
1590.67	0.421	0.172	0.837	18.685	4.427	1800A-185.457MeV-65mm1
1989.15	0.337	0.214	0.837	23.428	4.400	2400A-185.457MeV-65mm1

Figures 9 and 10 show the energy spread vs  $R_{56}$  for the 300A and 600A cases. For the 600A cases, the variation is dominated by the energy spread that must be induced for compression. For the 300A cases, this energy spread is much less because much less compression is required. Hence, at the higher values of  $R_{56}$  one begins to see an increase in energy spread, due to CSR. This is confirmed by 300A runs without CSR, which show a trend like that shown by the 600A cases.

**FIGURE 9. RMS energy spread vs  $R_{56}$  for 300A cases.**

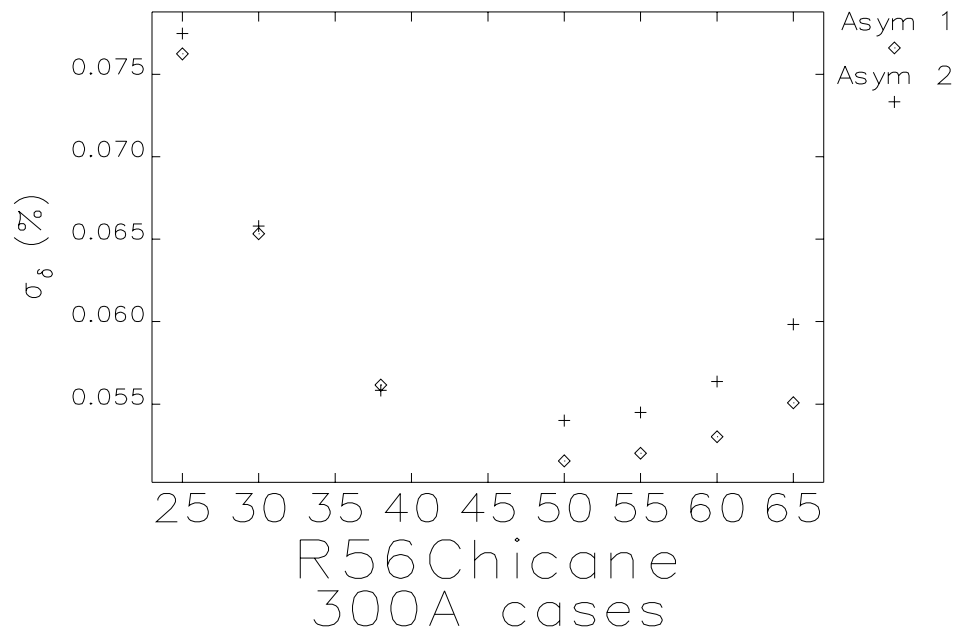
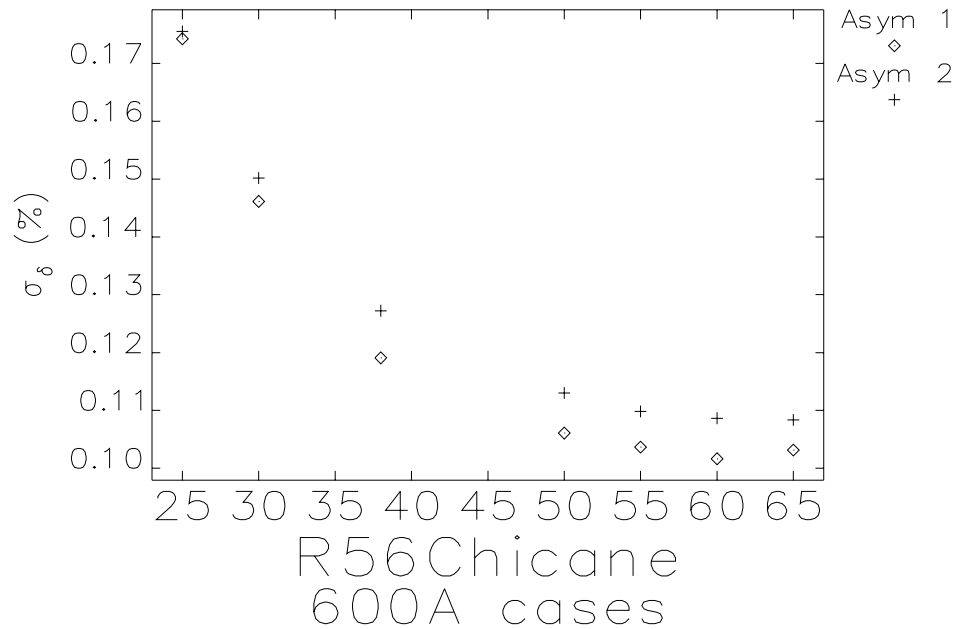


FIGURE 10. RMS energy spread vs  $R_{56}$  for 600A cases.



## 7.0 Tolerance Determination

There are two types of constraints that determine the tolerances on individual components. The first are those necessary for operation of the FEL. The second are those necessary for performance of CSR experiments and other characterizations of the compressor. All of the simulations reported on in this section included CSR, longitudinal wakes, and transverse wakes.

Steve Milton[2] has specified tolerances on the various beam parameters for the 300A and 600A cases based on the FEL physics. These tolerances are specified at the undulator, so I have translated them into equivalent tolerances at PB:FL:C1. This effectively ignores any errors downstream of PB:FL:C1, an assumption that Milton has accepted[2] (see Section 8.3, however). Tables 3 and 4 give the values for the 300A and 600A cases, respectively.

TABLE 3. Tolerances for 300A case translated to PB:FL:C1

Quantity	Nominal	Tolerance
Current	300A	-18/+22%
Normalized Emittance	5 um	-30/+34%
Beta	9.6m	-38/+46%
Energy Spread	0.1%	-100%/+42%
Energy	217MeV	+/-0.2MeV
x centroid	0	+/-185um
y centroid	0	+/-119um

**TABLE 3. Tolerances for 300A case translated to PB:FL:C1**

Quantity	Nominal	Tolerance
x' centroid	0	+/-34urad
y' centroid	0	+/-28urad

**TABLE 4. Tolerances for 600A case translated to PB:FL:C1**

Quantity	Nominal	Tolerance
Current	600A	-12/+14%
Normalized Emittance	5um	-20/+20%
Beta	9.6	-23/+23%
Energy Spread	1.5%	-13/+11%
Energy	456.5	+/-2MeV
x centroid	0	+/-185um
y centroid	0	+/-119um
x' centroid	0	+/-34urad
y' centroid	0	+/-28urad

These tolerances are to be understood as equivalent to standard deviations. I.e., Milton requires that 68% of the time, the beam should be within the specified windows.

Determination of component tolerances to meet these performance tolerances was done in several steps: parameter sweeps, quad jitter studies, misalignment/steering studies, and verification runs.

## 7.1 Parameter Sweeps

Individual parameter “sweeps” were done to obtain maximum allowable deviations for one parameter at a time. Parameters that were investigated in this fashion are: ganged strength error of B1+B2; ganged strength error of B3+B4; individual strength errors of B1, B2, B3, and B4; common transverse position of B2 and B3; longitudinal position of B4; phases of L2, L4, and L5; voltages of L2, L4, and L5; input beam charge, energy, and timing. These sweeps result in fairly stringent tolerances on phase and voltage. They are used to choose the least jitter sensitive  $R_{56}$  as far as RF parameters are concerned.

Of primary concern are the tolerances on rf phase and timing. For the configurations simulated, the phase tolerances for L2 are maximized for  $R_{56} = 65mm$  for both the 300A case and the 600A case. For these “best” cases, Table 5 summarize the “windows” for the rf phase, beam timing, and other quantities that influence primarily energy or energy

spread. Table 6 summarizes the windows for all cases for quantities that primarily influ-

**TABLE 5. Phase, voltage, timing, and related *windows* for “best” cases. See text for interpretation!**

<b>Case</b>	<b>bunch timing (ps)</b>	<b>charge (%)</b>	<b>input energy (%)</b>	<b>L2 phase (deg)</b>	<b>L4 phase (deg)</b>	<b>L5 phase (deg)</b>	<b>L2 volt. (%)</b>	<b>L4 volt. (%)</b>	<b>L5 volt. (%)</b>
300A	0.28	10	0.25	0.16	0.72	0.72	0.11	0.51	0.51
600A	0.14	6.0	1.1	0.15	1.5	1.5	0.33	1.5	1.5

**TABLE 6. Other parameter *windows* for all cases. See text for interpretation!**

<b>Case</b>	<b>2-dipole main (%)</b>	<b>dipole trim field (% of main)</b>	<b>B2+B3 x (mm)</b>	<b>B4 z (mm)</b>
300A	0.05	0.013	1.6	0.75
600A	0.07	0.017	2.0	1.0

ence beam position. I will use the smallest values from the two cases for these parameters to be more conservative.

These results must be interpreted with some care. The actual tolerance will be less than the “window” listed here, because the windows are determined by variation of a single parameter only. In general, the values in Table 5 are constrained by the final energy or final energy spread; the values in Table 6 are constrained by the horizontal trajectory.

Hence, the windows in Table 5 should be divided by  $\sqrt{9}$  while those in Table 6 should be divided by  $\sqrt{8}$  (two main supplies with two dipoles each, two trim supplies, with misalignment ignored, and with 50% of trajectory error assigned to other sources). These factors will change if the four dipoles are wired differently than assumed here (e.g., with four main supplies, or one main supply and three trims).

Because Milton’s specifications are to be interpreted as standard deviations, one obtains the RMS tolerance directly after dividing by the appropriate  $\sqrt{N}$  factor. This gives a 68% probability of being within the specification on any pulse. The tolerances derived from this procedure are quoted below, in Section 8.

It is worthwhile to note that the single-dipole tolerances are not the same for all the dipoles. The tolerance increases as one moves down the beamline, due to the existence of a waist in the horizontal beta function at B4. If the power supply configuration has (as assumed in this note) BM1 and BM2 on one supply, and BM3 and BM4 on another, then the trims should go on BM2 and BM4 in order to minimize the sensitivity to trim jitter. This would allow increasing the trim jitter tolerance listed in Table 6. However, in order to leave some room for jitter downstream of PB:FL:C1, I have not taken advantage of this opportunity.

### 7.1.1 Phase and Voltage Sensitivity

The phase and voltage sensitivity of the final energy can be computed analytically for comparison with simulations. This is a good way to check the simulations, but doesn't replace them as the analytical approach doesn't include bunch length, energy spread, emittance, and so on, which could in principle be relevant. The final energy is,

$$E_3 = V_2 \sin \phi_2 + 2V_4 \sin \phi_4$$

where  $V_2$  ( $2V_4$ ) and  $\phi_2$  ( $\phi_4$ ) are the voltage and phase of the pre- (post-) compressor linac. (The factor of two in front of  $V_4$  is used because there are two "sectors" with separate klystrons feeding the postcompressor linac. These sectors have the same nominal voltage and phase in the simulations.  $V_4$  represents the total voltage due to each klystron.) If the intermediate energy ( $E_2$ ) varies due to changes in  $V_2$  or  $\phi_2$ , then  $\phi_4$  will vary also, according to

$$\phi_4 = \phi_{4o} + \frac{2\pi R_{56}(V_2 \sin \phi_2 - V_{2o} \sin \phi_{2o})}{\lambda E_{2o}}$$

where the 'o' subscript indicates the unperturbed value and  $\lambda = 0.105m$  is the RF wavelength.

Using this result, one can compute the derivatives of  $E_3$  with respect to the rf parameters. For the precompressor linac, these give

$$\left. \frac{dE_3}{dV_2} \right|_o = F_1 \sin \phi_{2o}$$

and

$$\left. \frac{dE_3}{d\phi_2} \right|_o = F_1 V_{2o} \cos \phi_{2o}$$

where

$$F_1 = 1 + \frac{4\pi R_{56} V_{4o} \cos \phi_{4o}}{\lambda E_{2o}}$$

The comparable results for sensitivity to  $V_4$  and  $\phi_4$  are even more trivial, except that one must be careful of factors of two when comparing to simulations that vary only one of the two postcompressor sectors. I record the results here for easy reference

$$\left. \frac{dE_3}{2dV_4} \right|_o = \sin\phi_{4o}$$

and

$$\frac{dE_3}{2d\phi_4} = V_{4o} \cos\phi_{4o}$$

Figures 11 and 12 show the jitter sensitivity of the precompressor linac from these equations and from **elegant**, as a function of  $R_{56}$ . The agreement is quite good for the voltage sensitivity, and reasonably good for the phase sensitivity. Differences may be due to **elegant**'s use of an extended particle distribution or second-order effects in the compressor. Agreement between analysis and **elegant** for the sensitivity to  $V_4$  and  $\phi_4$  is very good; since these don't depend on the simulation of the compressor, I favor the latter explanation of the discrepancy. These results confirm that the best place to operate for reduced sensitivity is at the largest magnitude of  $R_{56}$ .

**FIGURE 11. Final energy sensitivity to precompressor linac voltage, from analytical expressions and elegant.**

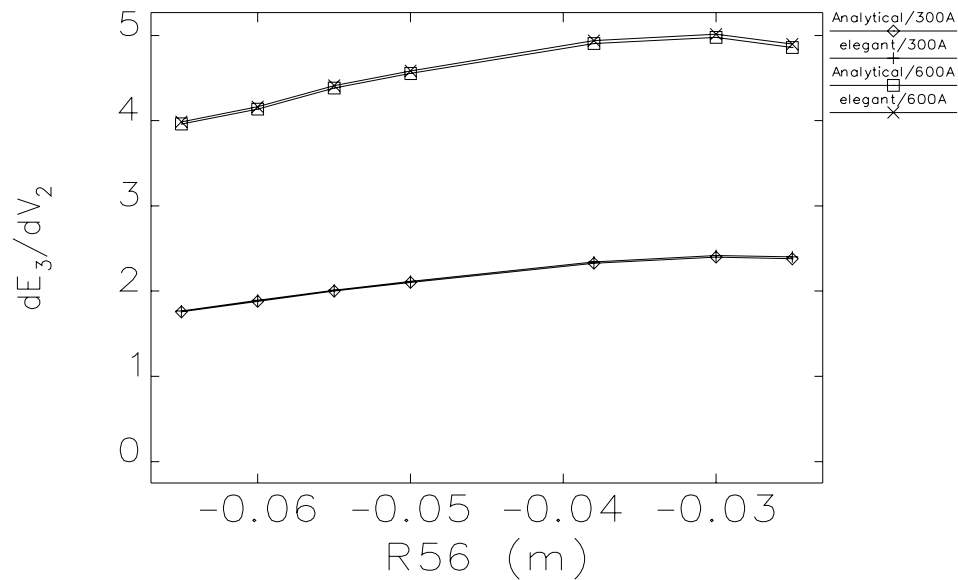
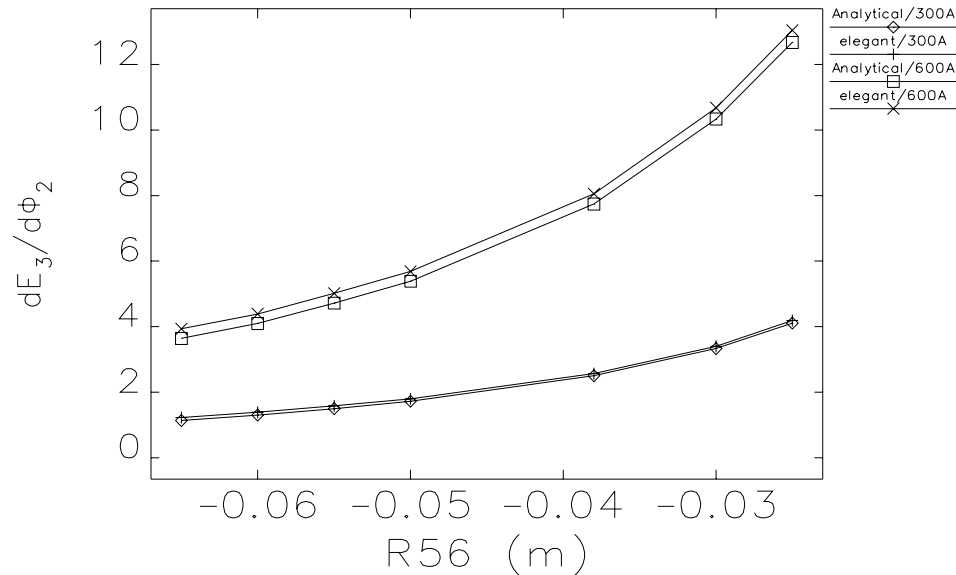


**FIGURE 12. Final energy sensitivity to precompressor linac phase, from analytical expressions and elegant.**



## 7.2 Quad Jitter

Quad jitter studies were done employing random errors on all quadrupole strengths. These are constrained by the beta function requirements in Tables 3 and 4, but (more strictly) by beta function requirements thought necessary for good operation and emittance measurement.

The principle measurement for diagnosing CSR is emittance measurement. Whatever technique we use will involve beam size measurements spaced over time (a few minutes). Hence, it is important that beam sizes do not drift appreciably during the measurements, either at the bunch compressor measurement station or the PAR bypass station. For the three screen measurement, a 1% variation in beamsize translates into a 1% error in emittance determination. A 1% variation in beamsize would result from a 2% variation in the beta function, for example. Ideally, I would like a 1% constraint on the beamsize variation, but think this will be too difficult. A 2.5% constraint (5% on beta functions) seems achievable and should allow us to resolve the effects we want to see.

For the “Bunch Compressor Lite” stage of the project, the requirement of highly accurate emittance measurements will be relaxed, and I use only the constraints based on Tables 3 and 4.

I performed quad jitter simulations for several levels of fractional strength error. For fractional errors of  $3 \cdot 10^{-4}$ , the 68% fractional range for the beta functions at PB:FL:C1 and L3:FS3 was at most 1.77%. The scaling of the beta errors with fractional strength errors

appears fairly linear, so holding the RMS fractional errors to  $4 \cdot 10^{-4}$  should hold the RMS beta function errors to 2.5%. For the BC Lite stage, scaling of simulation values from  $1 \cdot 10^{-3}$  gives a regulation requirement of  $3.5 \cdot 10^{-3}$ .

Table 7 gives the required supply regulation in amps, along with the maximum and minimum required currents. The latter two values were obtained from the matching results by adding a 10% margin to the range. In computing the regulation, I multiplied the fractional tolerance by the minimum current or by 30% (217MeV/700MeV) of the maximum current, whichever was greater. This largely prevents impossible regulation values due to very small currents. However, LTP:Q6 and LTP:Q7 get very small values; the values for LTP:Q8 should be used.

**TABLE 7. Quadrupole specifications for the final stage of the bunch compressor.**

QuadName	QuadType	Upper Current Limit (A)	Lower Current Limit (A)	Current Tolerance (A)	Bipolar ?
BYPQ1	PAR Bypass	15.7153	4.1176	0.0020	0
BYPQ2	PAR Bypass	16.3925	4.0374	0.0021	0
L1QM1	4Q6 R&D Magnetics	3.5655	3.1854	0.0014	1
L1QM2	4Q6 R&D Magnetics	4.3805	3.9698	0.0017	1
L1QM3	4Q6 R&D Magnetics	1.7952	1.6424	0.0008	1
L1QM4	4Q6 R&D Magnetics	3.0770	2.7977	0.0012	1
L1QM5	4Q6 R&D Magnetics	2.4885	2.2652	0.0010	1
L2:QM1	15Q15 Danfysik	7.5795	5.0898	0.0021	0
L2:QM2	15Q15 Danfysik	4.4469	2.5006	0.0011	0
L2:QM3	15Q30 Danfysik	11.3422	7.2184	0.0030	0
L2:QM4	15Q30 Danfysik	10.8141	6.9586	0.0029	0
L2:QM5	15Q30 Danfysik	21.2509	9.1174	0.0037	0
L2:QM6	15Q30 Danfysik	25.0943	10.2014	0.0042	0
L2:QM7	15Q30 Danfysik	102.0710	55.4298	0.0223	0
L2:QM8	15Q30 Danfysik	106.7055	58.7570	0.0236	0
L3:QM1	4Q6 R&D Magnetics	0.7394	0.0000	0.0002	1
L3:QM2	4Q6 R&D Magnetics	1.2803	0.0000	0.0003	1
L3:QM3	PAR Quad	80.7025	43.4438	0.0175	0
L3:QM4	4Q10 Danfysik	58.9428	33.9438	0.0137	0
L3:QM5	4Q10 Danfysik	80.5187	39.2977	0.0158	0
L3:QM6	4Q10 Danfysik	51.2841	27.5016	0.0111	0
LTP:Q10	LTP Alpha	3.0379	0.4186	0.0005	0
LTP:Q6	LTP Alpha	0.4927	0.0000	0.0002	0
LTP:Q7	LTP Alpha	0.3618	0.0000	0.0001	0

**TABLE 7. Quadrupole specifications for the final stage of the bunch compressor.**

<b>QuadName</b>	<b>QuadType</b>	<b>Upper Current Limit (A)</b>	<b>Lower Current Limit (A)</b>	<b>Current Tolerance (A)</b>	<b>Bipolar ?</b>
LTP:Q8	LTP Alpha	2.6352	0.3158	0.0004	0
LTP:Q9	LTP Alpha	3.4066	0.4783	0.0005	0
PL:QM11	15Q30 Danfysik	36.8188	13.1963	0.0054	0
PL:QM14	15Q30 Danfysik	37.4761	12.3991	0.0051	0
PL:QM17	15Q30 Danfysik	43.3604	12.8063	0.0053	0
PL:QM2	15Q30 Danfysik	72.4165	39.6866	0.0160	0
PL:QM20	15Q30 Danfysik	53.8389	14.9393	0.0066	0
PL:QM22	15Q30 Danfysik	46.8459	11.6785	0.0057	0
PL:QM24	15Q30 Danfysik	45.6453	10.6763	0.0056	0
PL:QM3	15Q30 Danfysik	142.8591	74.8205	0.0300	0
PL:QM4	15Q30 Danfysik	104.4668	52.1147	0.0209	0
PL:QM5	15Q30 Danfysik	28.0278	12.3093	0.0050	0
PL:QM8	15Q30 Danfysik	27.9188	10.4978	0.0043	0

### 7.3 Steering and Alignment

Steering studies were done with misaligned quadrupoles, dipoles, and beam position monitors (BPMs). The issue here is to limit emittance growth due to transverse wakes. Misalignments were performed relative to the ideal beam path in all cases. (An alternative would be to misalign the accelerating sections, then other elements relative to this.) All elements were misaligned at the same RMS level. Elements included in the misalignment were: quadrupoles (x, y); linac cavities and transverse wakes (x, y); dipoles (x, y, z, tilt); beam position monitors (x, y).

x, y, and z misalignment levels of 250um, 350um, and 450um were used. Tilt misalignments of the diopoles were 2mrad RMS, a number that should be readily achieved. The interpretation of the misalignment level is different for different types of elements. For magnets, it is the precision of placement of the magnetic center. For BPMs, it is the precision of placement of the electrical center. For RF elements, it is the precision of placement of the electrical center and apertures (which are assumed to move together). Hence, since there are various uncertainties in determining electrical and magnetic centers, the actual mechanical alignment tolerances for different elements may be different.

Using 100 random configurations for the standard 300A and 600A cases, I found that the 450um error level was acceptable. As expected, the horizontal emittance most showed the effect of misalignments. For the 1200A case, however, 450um was unacceptable in that 50% of the random configurations were outside the allowed limits. 350um was however, acceptable for the 1200A case.

These simulations are only a starting point for verification of alignment tolerances. In reality, because of the presence of steering magnets in the beamline and emittance-sensitive

diagnostics, the emittance growth due to misalignment can probably be tuned away. Provided that BPMs do not vary excessively (e.g., >100um), we should be able to reproduce the tuned condition from run to run. For this reason, the 350um is chosen as the specification for alignment tolerance. For 1200A or less, it should assure good performance without special tuning. For 1200A or more, some wakefield-based trajectory tuning may be required.

## 8.0 Tolerance Verification

Having determined the tolerances, it is necessary to verify them by randomization runs that combine multiple error sources. This checks, for example, the  $\sqrt{N}$  factors used to convert sweep windows to RMS tolerances. It also verifies that there are no surprises, like unacceptable trajectory jitter due to quadrupole strength jitter when there are misalignments.

### 8.1 Verification Runs for Power Supplies and Misalignment

These runs involve quadrupole jitter, corrector jitter, dipole jitter, steering, and misalignment. For the 300A case, 10 randomly misaligned configurations were created. For each of these configurations, 20 random jitter configurations were considered. The error levels are listed in Table 8.

**TABLE 8. Error levels used in verification runs for misalignment and magnet strength**

Quantity	Units	Error Level (RMS)
quadrupole K1	%	0.35
2-dipole strength	%	0.018
dipole trim strength	% of main	0.0037
corrector current	urad	1
alignment	um	350
dipole tilt	mrاد	2

There were no surprises found from these runs. The largest variations (relative to specifications) were in the x centroid position and slope. These were within the limits about 75% of the time.

### 8.2 Verification Runs for RF and Related Parameters

These runs involve RF phase, RF voltage, input beam timing, input beam energy, and input beam charge. The error levels used were based on Tables 5 and 6, with the appropriate  $\sqrt{N}$  factors, and are summarized in Table 9. (Note that I mistakenly used  $\sqrt{10}$

instead of  $\sqrt{9}$  here, since I initially included a dipole-related term. This makes a 5% difference on the conservative side.)

Runs were performed for the standard 300A and 600A cases, with 100 random configurations in each case. These runs clearly confirm the tolerance values. In the both cases, only

**TABLE 9. Error levels used in verification runs for rf and related parameters.**

Quantity	Units	Error Level (RMS)
rf phase, L2	degrees	0.047
rf voltage, L2	%	0.034
rf phase, L4/L5	degrees	0.23
rf voltage, L4/L5	%	0.16
arrival time at L2	ps	0.044
input energy at L2	%	0.078 (at 43MeV)
input charge	%	1.9

the final energy and energy spread are strongly affected. For the 300A case, 80% of the configurations are within the limits, while for the 600A case 98% are within the limits. In the 300A case, the final energy is the determining factor, while in the 600A case the energy spread is the determining factor. In any case, the tolerances in Table 9 are somewhat too tight. I decided to relax the L2 rf phase and the arrival time at L2, as these are the hardest to meet. The final tolerances are listed in Table 10.

**TABLE 10. Final tolerance values for rf and related parameters**

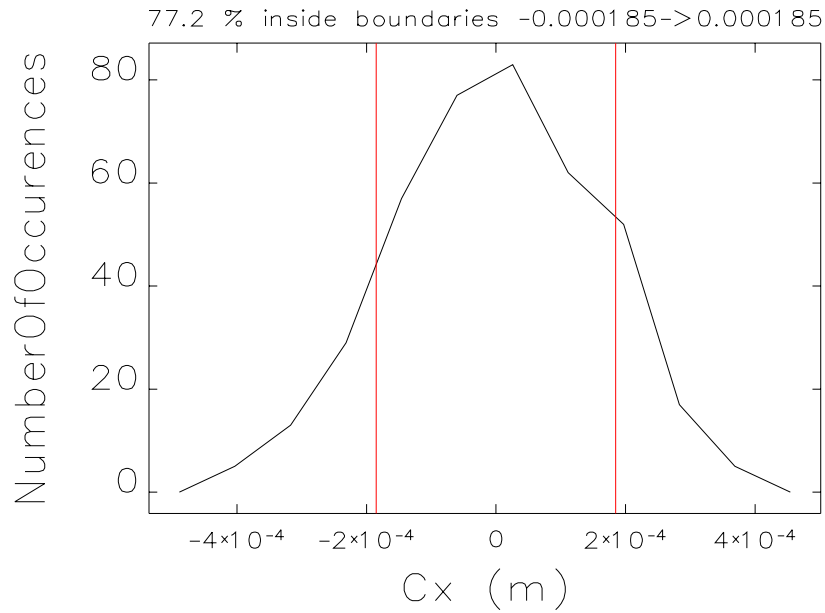
Quantity	Units	Error Level (RMS)
rf phase, L2	degrees	0.080
rf voltage, L2	%	0.034
rf phase, L4/L5	degrees	0.23
rf voltage, L4/L5	%	0.16
arrival time at L2	ps	0.080
input energy at L2	%	0.078 (at 43MeV)
input charge	%	1.9

### 8.3 All-Inclusive Verification Runs

In these runs, the error levels of 8.1 and 8.2 are combined. Specifically, I used the values from Tables 8 and 10. This is a final check to ensure that no unexpected cross-talk is present between the various types of errors. For the 300A and 600A cases, 20 misaligned configurations were used. Each of these configurations was used 20 times with instances of the other errors, for a total of 400 configurations.

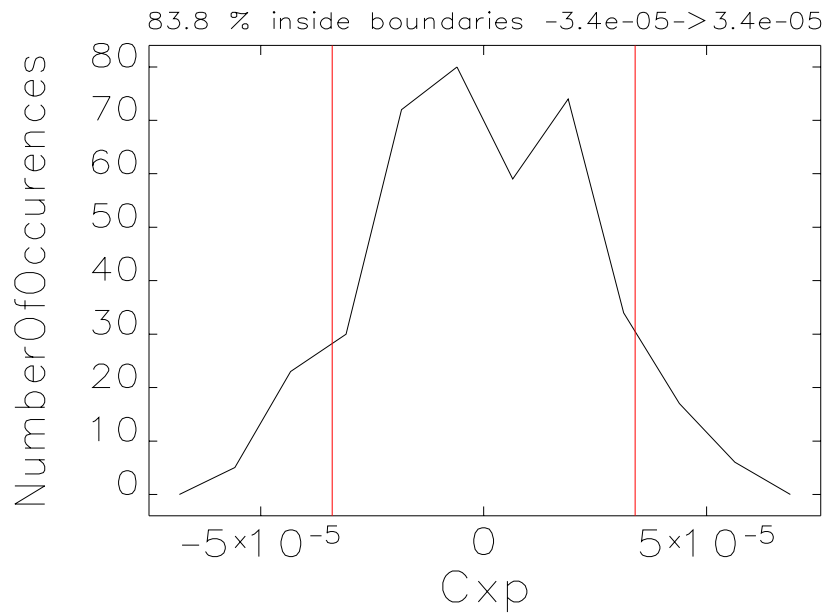
No surprises were found. The tolerances in Tables 8 and 10 are correct. The figures below show some of the data from the 300A runs.

**FIGURE 13. Distribution of the x centroid at PB:FL:C1 for 300A case.**



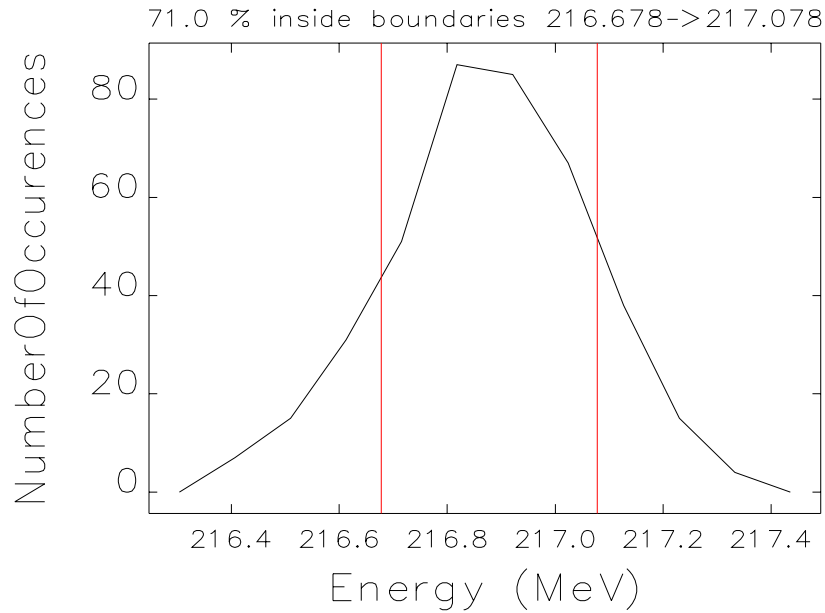
/home/oxygen26/BORLAND/aps/bunchComp/VaryL3/optics4.7/310A-140.217MeV-65mm2/allJitter/relax4

**FIGURE 14. Distribution of the x' centroid at PB:FL:C1 for 300A case.**



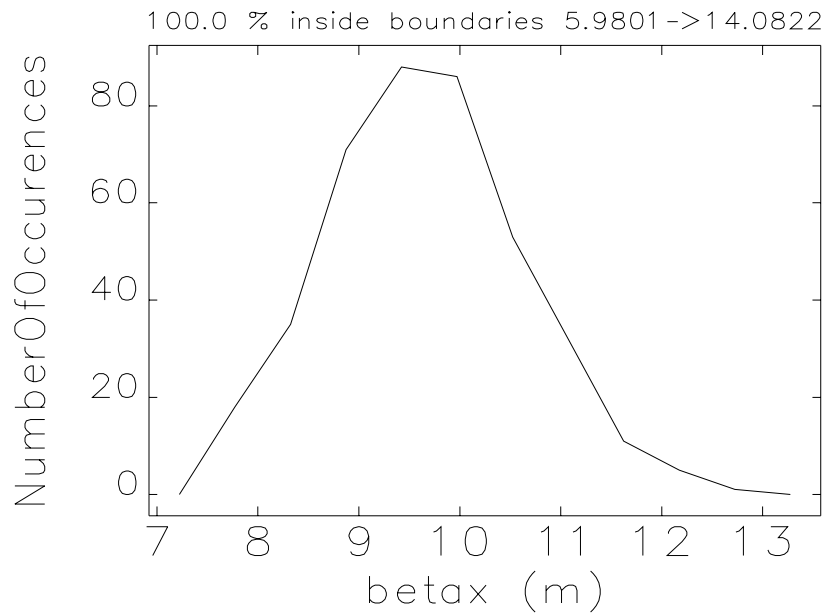
/home/oxygen26/BORLAND/aps/bunchComp/VaryL3/optics4.7/310A-140.217MeV-65mm2/allJitter/relax4

**FIGURE 15. Distribution of the final energy for the 300A case.**



/home/oxygen26/BORLAND/aps/bunchComp/VaryL3/optics4.7/31 0A-1 40.21 7MeV-65mm2/allJitter/relax4

**FIGURE 16. Distribution of the horizontal beta function at PB:FL:C1 for the 300A case.**



/home/oxygen26/BORLAND/aps/bunchComp/VaryL3/optics4.7/31 0A-1 40.21 7MeV-65mm2/allJitter/relax4

## 9.0 Acknowledgements

The author wishes to acknowledge many useful discussions with Paul Emma, John Lewellen, and Steve Milton in the course of developing the bunch compressor design. Eliane Lessner and Horst Friedsam were helpful in getting the element positions for the lattice.

## 10.0 References

- [1] P. Emma, V. Bharadwaj, “Bunch Compressor Options for the LEUTL Facility at the APS”, unpublished.
- [2] S. Milton, private communication.
- [3] P. Emma, private communication.
- [4] E. L. Saldin, et. al., “On the coherent radiation of an electron bunch moving in an arc of a circle,” NIM A 398 (1997) 392.
- [5] E. Forest, “Canonical Integrators as Tracking Codes,” in *Physics of Particle Accelerators*, AIP Conference Proceedings 184, p 1112.
- [6] W. Press, et. al., *Numerical Recipes in C*, 2nd Edition, p 650.
- [7] K. L. Brown, “Single Element Optics,” in *Handbook of Accelerator Physics and Engineering*, A. Chao and Maury Tigner, eds, p 56.
- [8] H. Wiedemann, “Bending Magnet Radiation,” in *Handbook of Accelerator Physics and Engineering*, A. Chao and Maury Tigner, eds, p 184.